Journal of Alloys and Compounds 509 (2011) 5119–5126

Contents lists available at ScienceDirect

Journal of Alloys and Compounds

journal homepage: www.elsevier.com/locate/jallcom

Synthesis, structural and electrical characterization of Sb^{3+} substituted spinel nickel ferrite ($NiSb_xFe_{2-x}O_4$) nanoparticles by reverse micelle technique

Muhamamd Naeem Ashiq[a,*], Muhammad Fahad Ehsan[a], Muhammad Javed Iqbal[b], Iftikhar Hussain Gul[c]

[a] Department of Chemistry, Bahauddin Zakariya University, Multan 60800, Pakistan
[b] Department of Chemistry, Quaid-i-Azam University, Islamabad 45320, Pakistan
[c] School of Chemical and Materials Engineering (SCME), National University of Sciences and Technology (NUST), H-12 Islamabad, Pakistan

ARTICLE INFO

Article history:
Received 29 November 2010
Received in revised form 26 January 2011
Accepted 27 January 2011
Available online 2 March 2011

Keywords:
Nanoferrites
Metal-to-semiconductor transition temperature
Mossbauer Spectroscopy
Electrical properties
AFM
X-ray diffraction

ABSTRACT

Spinel nickel ferrite with nominal composition $NiFe_{2-x}Sb_xO_4$ (where $x = 0.0$, 0.2, 0.4, 0.6, 0.8 and 1) has been synthesized by the reverse microemulsion method. The samples synthesized were characterized by XRD, FTIR, TGA/DTGA, SEM, AFM, Mossbauer Spectroscopy and DC electrical resistivity measurements. The XRD analysis confirmed the formation of single spinel phase and the crystallite size was found to be in the range of 8–38 nm. The particle size of the synthesized samples was also confirmed by the AFM and SEM which was found in the range of 5–45 nm and 10–45 nm, respectively and this size is small enough for obtaining the suitable signal-to-noise ratio in high density recording media. The Mossbauer spectra of samples showed two well-resolved Zeeman patterns corresponding to A and B sites and also observed a doublet at higher substitution. The DC electrical resistivity showed an interesting behavior with temperature and observed a metal-to-semiconductor transition temperature (T_{M-S}) which suggests that the material can be applied for switching applications. The resistivity increases with the increase in Sb-content and it suggests that the material can be fruitfully used for applications in microwave devices.

1. Introduction

Nanotechnology deals with the structures of ranges between 1 and 100 nm at least in one dimension, where unique phenomenon enables some vital applications [1]. Nanomaterials are known to have interesting physical and chemical properties which are different from that of their bulk counterparts, which is due to their extremely small size and very large surface area [2,3].

Spinel ferrites nanomaterials have been widely used in several important technological fields such as magnetic drug delivery, ferrofluids, microwave devices and magnetic high-density information storage media [4–7] for last few years due to their useful physical, electrical and magnetic properties. These materials are preferred over other magnetic materials i.e. alloys because of their excellent chemical stability, good mechanical hardness, high electrical resistivity and reasonable cost [8–11]. Amongst these spinel ferrites, the inverse spinel ferrites are of great interest in particular for their high saturation magnetization and high magnetocrystalline anisotropy [12]. The properties of the synthesized nanoparticles directly depend upon the composition and microstructure of the surface, which are influenced by their method of preparation. Many methods have been reported for the synthesis of nanocrystalline $NiFe_2O_4$ such as gas condensation, aerosol reduction, chemical precipitation, sol–gel processing, thermal decomposition of organometallic precursors and continuous hydrothermal processing [13–16]. Although the nanoscale ferrites are synthesized by these methods but time and again the quality of nanoparticles is reduced in many cases (a large size distribution is reported and size control is arbitrary). In many of these methods, the variation in size is achieved through the post-synthesis annealing at various temperatures. In order to correlate the effect of size with the changes in the magnetic properties, it is critical to have a synthesis method that allows for the control over the nanoparticles size and yields nanoparticles with a narrow size distribution [16]. Microemulsion approach is suitable for such purposes.

In present work, we report the synthesis of nanocrystalline nickel ferrite and their derivatives by the reverse microemulsion method. The structural and electrical properties of the synthesized materials are reported. The aim of the present work is to enhance the electrical resistivity of the materials and to make these materials useful for applications in microwave devices as these devices require highly sensitive materials.

* Corresponding author. Tel.: +92 3009879344; fax: +92 619210083.
E-mail address: naeemashiqqau@yahoo.com (M.N. Ashiq).

0925-8388/$ – see front matter © 2011 Elsevier B.V. All rights reserved.
doi:10.1016/j.jallcom.2011.01.193

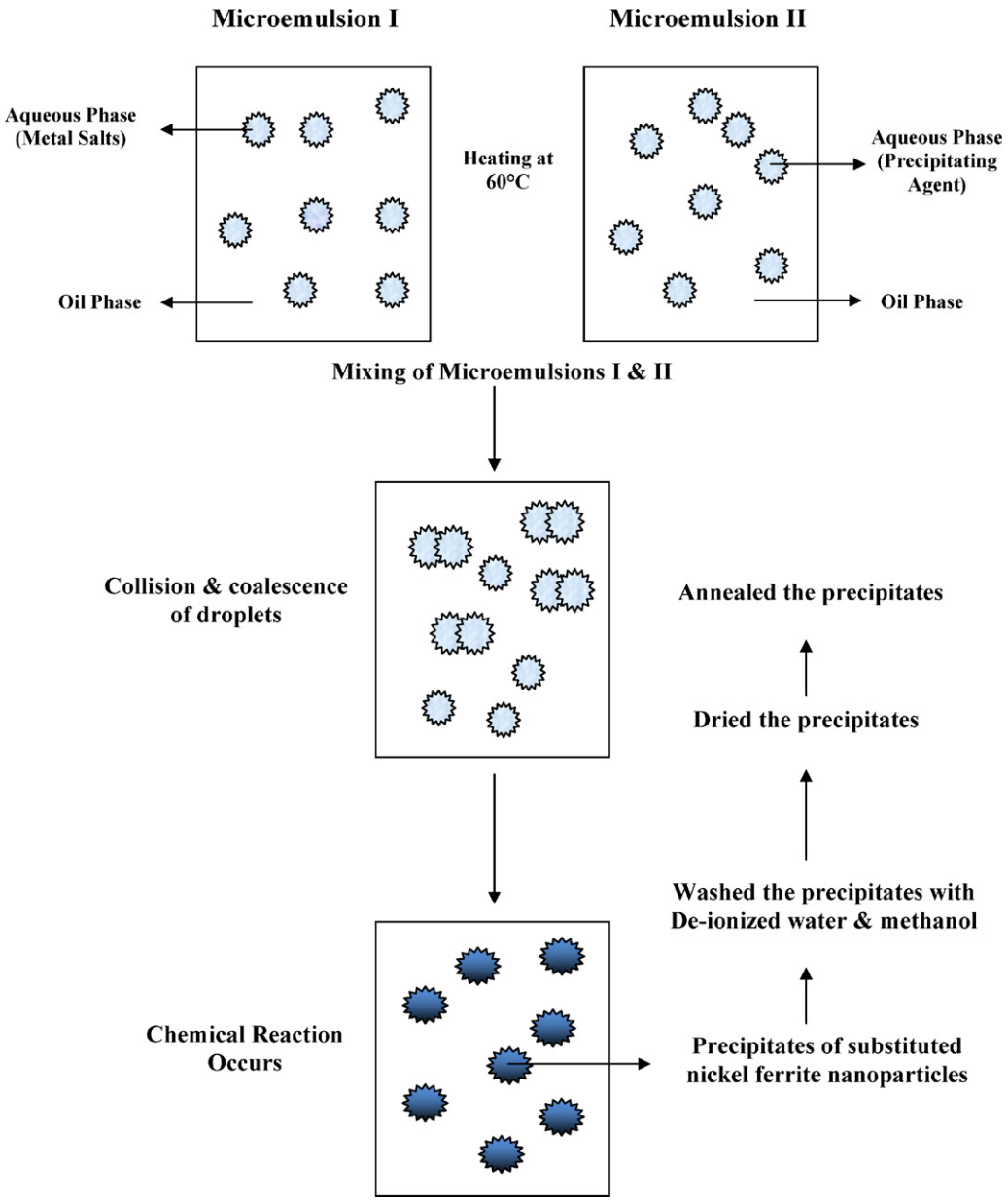

Fig. 1. Schematic diagram for the microemulsion method.

2. Experimental

The chemicals used in the synthesis of substituted nickel ferrite nanoparticles are $Fe(NO_3)_3{\cdot}9H_2O$ (Riedel-de Haen, 97%), $Ni(NO_3)_2{\cdot}6H_2O$ (Merck, >99%), $SbCl_3$ (Merck, 99%), CTAB (Merck, 97%) as a surfactant, 1-butanol (Fluka, 98%) as a co-surfactant, iso-octane (BDH, 99%) as an oil phase, NH_3 (Fisher Scientific, 35%) as a precipitating agent and methanol (Merck, 99%) as washing agent.

For the synthesis of substituted nickel ferrites two microemulsions (microemulsion I and microemulsion II) were prepared. Microemulsion I consists of iso-octane as an oil phase, 0.6 M CTAB as the surfactant, 1-butanol as the co-surfactant, 0.1 M $Ni(NO_3)_2{\cdot}6H_2O$, $(0.2-x)$ M $Fe(NO_3)_3{\cdot}9H_2O$ and (x) M $SbCl_3$ (where $x = 0.00$, 0.02, 0.04, 0.06, 0.08 and 0.1) was stirred on the magnetic hot plate at 60 °C until it formed a clear solution. Microemulsion II consists of the same materials except the aqueous phase of the metal salts which was replaced by the aqueous phase of 2 M NH_3 solution and was obtained by the same protocol. Microemulsion II was then added drop wise to microemulsion I under constant stirring that resulted in the formation of $NiFe_{2-x}Sb_xO_4$ precipitates. After that the precipitates were washed with deionized water and finally with methanol. Then the precipitates were dried in an oven at 150 °C and finally annealed at 800 °C for 8 h. The schematic diagram for the microemulsion process is shown in Fig. 1. The samples thus synthesized were characterized using different characterization techniques.

2.1. Characterization

The TGA/DTG analysis was carried out to investigate the structural changes with temperature by thermogravimetric analyzer Mettler-Toledo system (TGA/SDTA 851e) operating at a heating rate of 10 °C min^{-1}. The FTIR spectrophotometer (8400 Shimadzu, Japan) was used to investigate the formation of nickel spinel ferrites. The powder X-ray diffraction (XRD) analysis was performed for the purity and phase formation by JEOL JDX-60PX diffractometer which uses Cu K_α as a radiation source. SEM (JEOL, JSM-6490A) and AFM (JEOL, JSPM-5200) were used to investigate the particle size and surface structure of the synthesized materials. Mossbauer analysis is carried out using SEECo MSCI Mossbauer spectrometer with NRD-I 43-DMB, CN2 cryostat, running in constant acceleration mode with a source of 50 mCi Co^{57} in Rh matrix. The model of Lorentzian multiplet analysis was used to analyze the data obtained. The DC electrical resistivity measurements were carried out using two point probe method. Pellets of 13 mm diameter and 2 mm thickness were used for DC electrical resistivity measurements.

2.2. Calculations

XRD data was used to calculate the various parameters i.e. lattice constant (a), cell volume (V), X-ray density ($\rho_{X\text{-ray}}$) and crystallite size (D) are calculated using

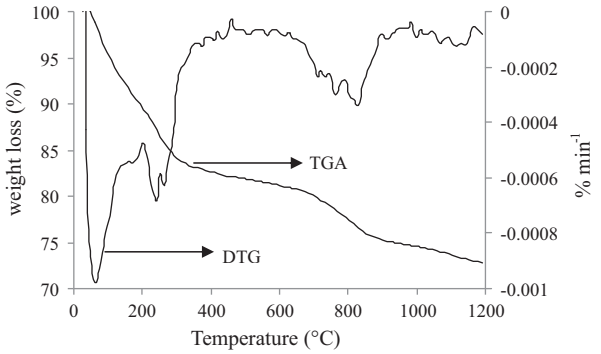

Fig. 2. TGA/DTG curves for the unannealed sample of $NiFe_2O_4$ synthesized by the reverse microemulsion method.

following formulae [17]:

$$\frac{1}{d^2} = \frac{h^2 + k^2 + l^2}{a^2} \quad (1)$$

$$V = a^3 \quad (2)$$

$$\rho_{\text{X-ray}} = \frac{ZM}{N_A V} \quad (3)$$

$$D = \frac{K\lambda}{\beta \cos\theta} \quad (4)$$

where λ is the X-ray wavelength, β the full width at half maxima, K the constant, Z the number of formula units in a unit cell, M the molecular mass of the sample and N_A is the Avogadro's number.

The DC electrical resistivity (ρ) is measured using the following equation:

$$\rho = \frac{RA}{l} \quad (5)$$

where R is the resistance, A the area and l is the length of the sample.

The drift mobility (μ_d) is calculated from the DC electrical resistivity data using the following equations [17]:

$$\mu_d = \frac{1}{ne\rho} \quad (6)$$

where e is the charge on electron, ρ the resistivity and n is the concentration of charge carriers which can be calculated by the following equation:

$$n = \frac{N_A \rho_m Q}{M} \quad (7)$$

where N_A is the Avogadro's number, ρ_m the measured density, Q the number of iron atoms in the chemical formula of the materials and M is the molar mass of the sample.

3. Results and discussion

Fig. 2 shows the TGA/DTG curve for an unannealed sample of $NiFe_2O_4$. The curve shows weight losses at 100, 300, 670 and 880 °C. Almost 16% of the weight loss at 100 °C is due to the loss of water from the sample. The weight loss at 300 °C is due to the decomposition and oxidation of organic substances i.e. surfactant. The peaks at 670 and 880 °C are attributed to the conversion of hydroxides of different metals into oxides and the formation of spinel nickel ferrite, respectively.

The FTIR spectra were recorded in the range of 4000–400 cm^{-1} for both annealed and unannealed samples and are shown in Fig. 3. This FTIR spectrum has four absorption bands at 450, 620, 1390 and 3420 cm^{-1} for the unannealed sample (Fig. 3a). Waldron [18] reported that the higher absorption band at ≈600 cm^{-1} corresponds to the intrinsic vibrations of the tetrahedral complexes and lower absorption band at ≈450 cm^{-1} is attributed to the vibrations of the octahedral complexes. The first two absorption bands at 450 and 650 cm^{-1} correspond to the metal–oxygen intrinsic stretching vibrations at the octahedral site, $M_{\text{octa}} \leftrightarrow O$ and tetrahedral metal–oxygen stretching, $M_{\text{tetra}} \leftrightarrow O$, respectively [18,19]. The absorption band at 1390 cm^{-1} is attributed to the stretching vibration of N–O in nitrate ion [20] indicates the presence of nitrates in the sample. The band at 3420 cm^{-1} corresponds to O–H stretching vibration in water, indicating the presence of moisture in the sample. The FTIR spectrum of the annealed $NiFe_2O_4$ is shown in Fig. 3(b). There are only two absorption bands at 420 cm^{-1} and 600 cm^{-1} which correspond to the octahedral and tetrahedral metal–oxygen stretching vibrations in the spinel compounds, respectively.

The powder XRD patterns for all the samples synthesized by reverse microemulsion method are shown in Fig. 4. It is observed that all the peaks perfectly match with the standard pattern (ICSD-00-003-0875) which indicates that there is no impurity in the sample i.e. the synthesized samples are in single spinel phase. The XRD data was used to calculate different parameters such as crystallite size (D), lattice constant (a), cell volume (V), X-ray density (ρ_x) and porosity (P) using Eqs. (1)–(5) and their values are given in Table 1.

The crystallite size (D) is found to be in the range of 8–38 nm which is much smaller as compared to 25–43 nm, 40–75 nm, 45 nm reported earlier by different workers for the spinel ferrites synthesized by the combustion method, sol–gel method, solid state reaction method and co-precipitation method, respectively [21–24]. It has been reported that the crystallite size below 50 nm are useful in obtaining the suitable signal-to-noise ratio in the high density recording media [25]. In the present study the crystallite size (8–38 nm) is below 50 nm, so the materials can be useful in obtaining suitable signal-to-noise ratio in high density recording media.

The values of lattice constant (a) and cell volume (V) are found to increase with the increase in the antimony content which is attributed to the larger ionic radius of Sb^{3+} (0.76 Å) as compared to Fe^{3+} (0.64 Å). The X-ray density is also found to increase with antimony content up to $x = 0.6$ and then decreases. The increase in the X-ray density is due to the greater molecular mass of Sb (121.76 g mol^{-1}) than that of Fe (58.85 g mol^{-1}) as the X-ray density is directly related to the molecular mass of the samples (Eq. (3)). The X-ray density is also inversely related to the cell volume of the sample and the decrease in ρ_x above $x = 0.6$ is owing to the sudden higher increase in the value of cell volume.

The morphology and the particle size of the samples were determined by scanning electron microscopy (SEM). The SEM images of the substituted $NiFe_{2-x}Sb_xO_4$ (where $x = 0.0$, 0.2, 0.4, 0.6, 0.8 and 1) are shown in Fig. 5(a–f). These figures indicate that the nanocrystalline nickel ferrites are spherical in shape and are uniformly distributed and some of the particles are also agglomerated. The average grain size determined by the SEM images was found to be in the range of 10–45 nm for the samples. The SEM micrographs clearly show that the surface is less smooth for the samples with $x = 0.0$–0.4 and also has some shaded areas due to voids Fig. 5(a–c), But as the substitution is increased, the material becomes more homogeneous and monodispersed.

The particle size of the samples synthesized by the reverse microemulsion method is also observed by the atomic force microscope (AFM). Complimentary information about the surface microstructure of the substituted nickel ferrites is obtained from the three-dimensional AFM images. Fig. 6(a–d) shows the AFM images of the substituted nickel ferrites nanoparticles $NiSb_xFe_{2-x}O_4$ (where $x = 0.0$, 0.2, 0.4, 0.6, 0.8 and 1, respectively). It can be seen from Fig. 6(a) that particles are spherical with the average size less than 50 nm. These images show that all the samples have uniform morphology having average size in the range of 5–45 nm.

The Mossbauer spectra of the nickel ferrites are recorded at room temperature in the absence of magnetic field and are shown in Fig. 7. The observed two sextets are due to Fe^{3+} at tetrahedral site (A-site) and the presence of Fe^{3+} at the octahedral site (B-site). Both the sextets are attributed to the magnetic hyperfine interactions of the Zeeman pattern [27]. One doublet also appears

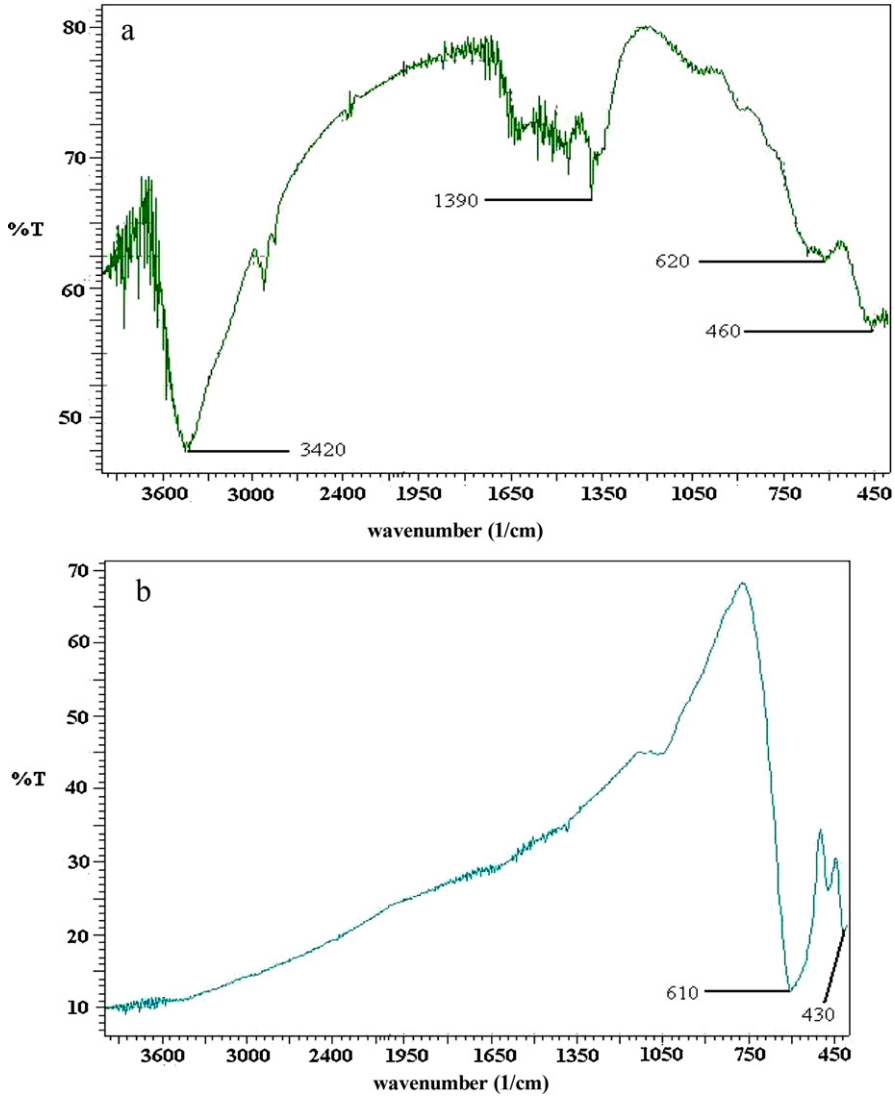

Fig. 3. FTIR spectra of nickel ferrite (a) unannealed and (b) annealed.

at higher antimony content for $x = 0.4$ and $x = 0.8$. The presence of this doublet may be attributed to the decrease in the concentration of Fe^{3+} at one of the two active sites in cubic spinel ferrites.

The chemical shift (CS), quadrupole splitting (QS), hyperfine interaction (H) and the relative area (A) calculated from the fitting of the spectra are given in Table 2. The chemical shift results from the electrostatic interaction between the charge distribution of the

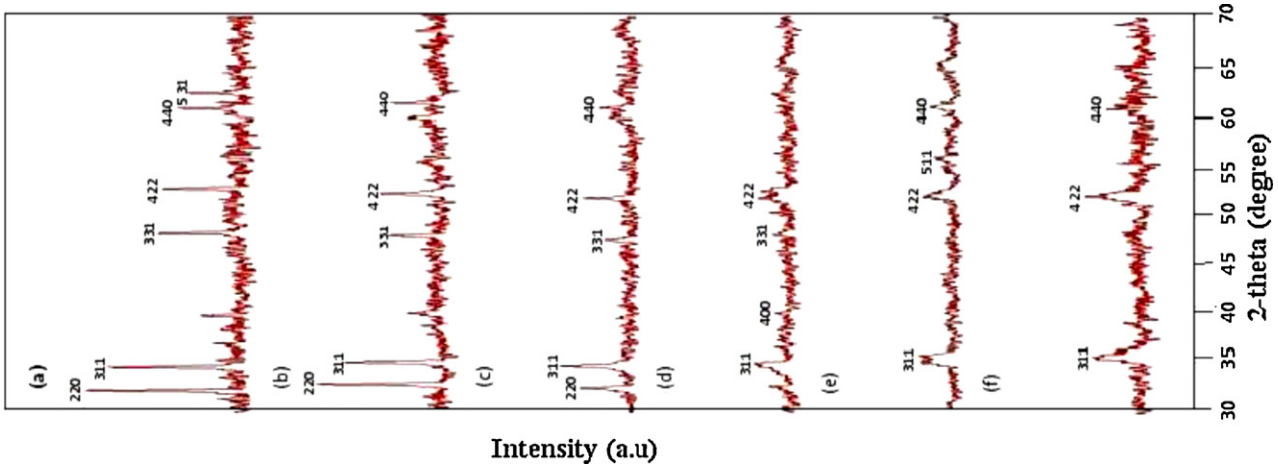

Fig. 4. Indexed XRD patterns for $NiFe_{2-x}Sb_xO_4$ (a) $x = 0.0$, (b) $x = 0.2$, (c) $x = 0.4$, (d) $x = 0.6$, (e) $x = 0.8$ and (f) $x = 1.0$.

Table 1
Crystallite size (D), lattice constant (a), cell volume (V), X-ray density (ρ_x), porosity (P), electrical resistivity (ρ) and drift mobility (μ_d) of $NiFe_{2-x}Sb_xO_4$ (where $x = 0.0$, 0.2, 0.4, 0.6, 0.8 and 1.0) ferrite nanoparticles.

Parameters	$x = 0.0$	$x = 0.2$	$x = 0.4$	$x = 0.6$	$x = 0.8$	$x = 1.0$
Crystallite size (D) (nm)	37.60	24.48	28.16	9.55	8.74	10.48
Lattice constant (a) (Å)	8.18	8.23	8.24	8.31	8.46	8.72
Cell volume (V) (Å^3)	550.50	559.60	561.40	572.90	605.20	666.70
X-ray density (ρ_x) (g cm^{-3})	5.73	5.94	6.24	6.36	6.31	6.12
Drift mobility (μ_d 10^{-11}) (cm^2 V^{-1} s^{-1})	2.29	1.85	1.41	1.30	1.19	1.51
Electrical resistivity (ρ 10^7) (Ω cm)	1.46	2.42	3.37	4.44	5.50	6.41
T_{M-S} (°C)	–	110	110	120	120	130

nucleus and those electrons that have finite probability of being found in the region of the nucleus. Only s-electrons have this finite probability and hence are responsible for this electrostatic interaction. The chemical shift is a physical parameter to determine the valency of the Mossbauer atom e.g. ferrous (Fe^{2+}) and ferric (Fe^{3+}) have electronic configuration of ($3d^6$) and ($3d^5$), respectively. The ferrous ions have lesser s-electron density at the nucleus because of the greater number of d-electrons. This produces a positive CS that is greater in ferrous ions than in ferric. The chemical shift for the A-site is smaller than that for the B-site (Table 2). It is already known

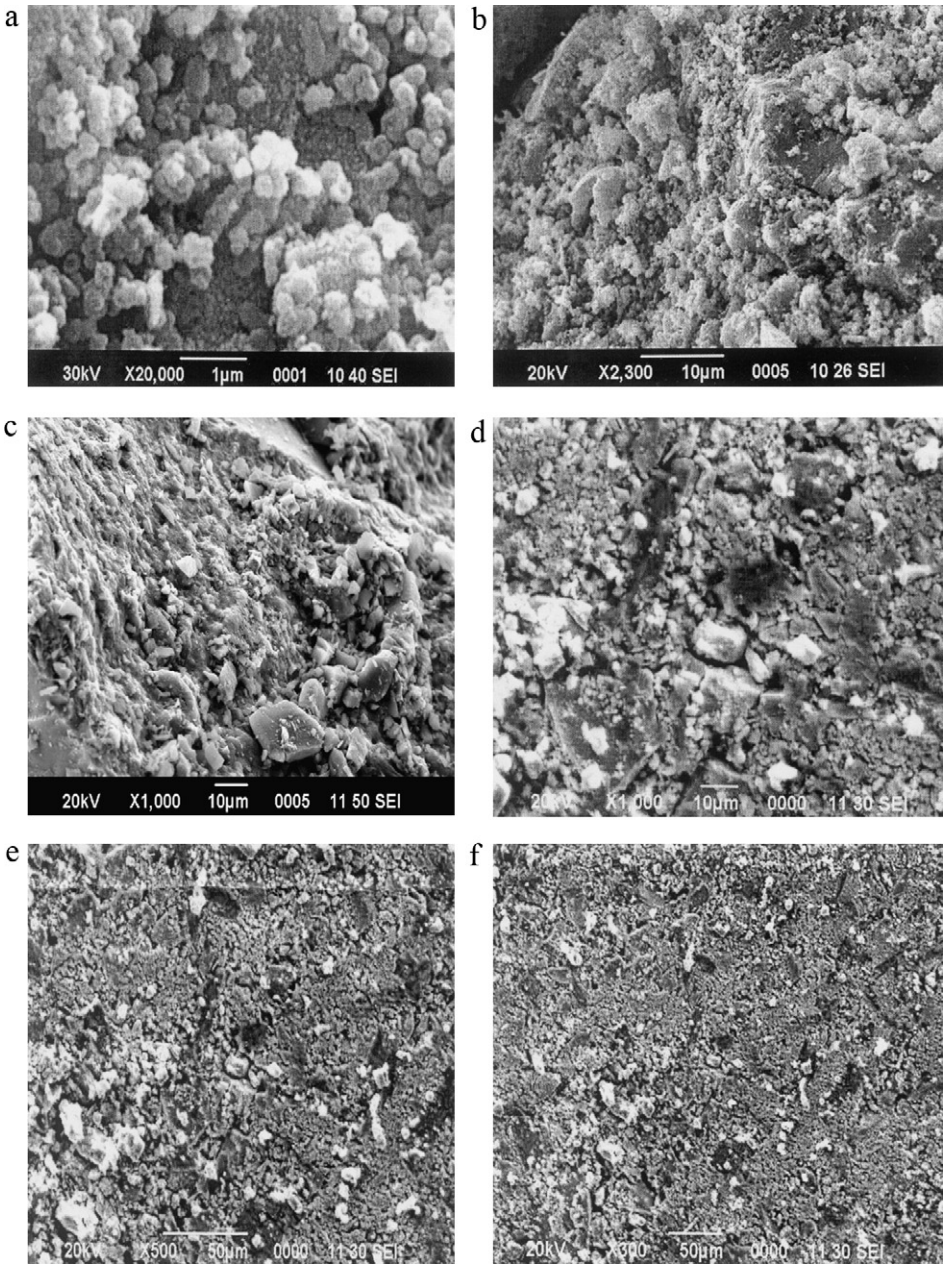

Fig. 5. SEM images with magnification power for nickel nanoferrites (a) $x = 0.0$ (×20,000), (b) $x = 0.2$ (×2300), (c) $x = 0.4$ (×1000), (d) $x = 0.6$ (×1000), (e) $x = 0.8$ (×500) and (f) $x = 1.0$ (×300).

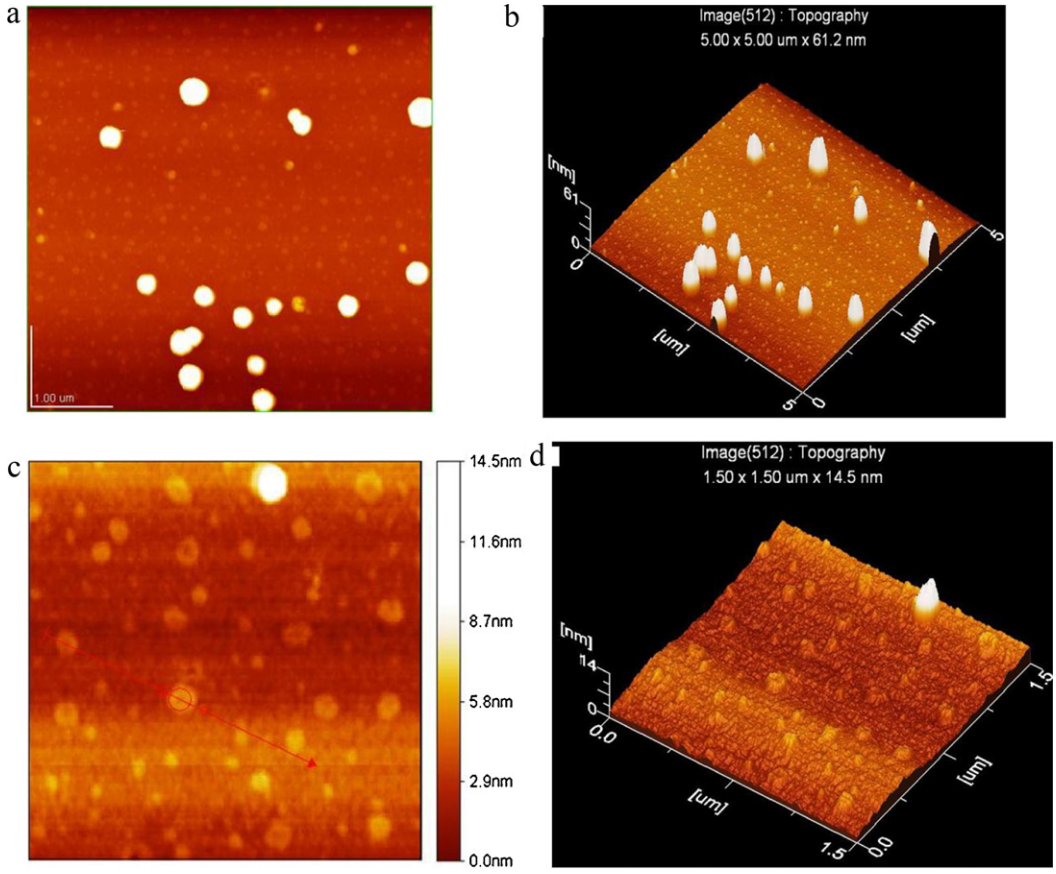

Fig. 6. AFM images for substituted nickel ferrite (a) $x = 0.0$, (b) $x = 0.2$, (c) $x = 0.6$ and (d) $x = 1.0$.

that the CS is more for the octahedral site (B-site) than that of the tetrahedral site (A-site) because of the fact that in the cubic spinel ferrites the separation of Fe^{3+}–O^{2-} bond is larger for the B-site as compared to that of the A-site, due to which the overlapping of the Fe^{3+} orbital is smaller at B-sites and thus a larger CS and hence more s-electron density emerges at B-sites [28].

It has been reported that the values of CS for Fe^{3+} ions lie in the range of 0.1–0.5 mm/s, while for Fe^{2+} ions these values lie in the range of 0.6–1.7 mm s^{-1} [29]. By comparing our results from Table 2 with the above mentioned, it can be concluded that the CS values indicate that the two sextets in the present study are due to Fe^{3+} only. The CS values indicate that iron is in Fe^{3+} state.

The non-zero quadrupole splitting is found in the present study which is attributed to the presence of the chemical disorders. These chemical disorders produce an electric field gradient (EFG) of varying magnitudes, sign, symmetry and directions, and hence results in the distribution of the quadrupole splitting. In the present studied samples, a paramagnetic doublet also appears within the sextet with an increase in the antimony content for $x = 0.4$ and $x = 0.8$ which is attributed to the interaction of the electric field gradient with the quadrupole moment of Fe^{57} nucleus and reduction in the magnetic interactions between Fe ions due to substitution of antimony.

The hyperfine interaction (H) at A and B sites for the synthesized materials is given in Table 2. The hyperfine interaction at A-site is found to decrease from 486.4 to 452.9 kOe, whereas at B-site it decreases from 507.4 to 473.9 kOe as the substitution of antimony increases from $x = 0.0$ to $x = 0.8$. In most of the ferrites B-site hyperfine interaction is generally larger than A-site, which is attributed to the dipolar field resulting due to deviation from cubic symmetry and covalent nature of tetrahedral bond [30]. The relative area (A) is found to increase at A-site from 4.05% to 22.7% but at B-site it decreases from 95.95% to 50.1% (Table 2) which may be attributed to the octahedral site preference of antimony.

By concluding from all the results and above mentioned discussions we can see that the values of the parameters such as isomer/chemical shift (CS), quadrupole splitting (QS), hyperfine interaction (H) and the relative area (A) decrease more intensely

Table 2
Isomer/chemical shift (CS), quadrupole splitting (QS), hyperfine interaction (H) and relative area (A).

Parameters	Bond area	$x = 0.0$	$x = 0.4$		$x = 0.8$	
CS (mm/s)	A-site	0.292	0.273		0.335	
	B-site	0.383	0.384		0.374	
QS (mm/s)	A-site	0.135	−0.122		0.087	
	B-site	−0.1005	−0.083	Doublet	−0.659	Doublet
H (kOe)	A-site	486.4	462.5		452.9	
	B-site	507.4	487.7		473.9	
A (%)	A-site	4.05	19.35		22.7	
	B-site	95.95	71.77		50.1	

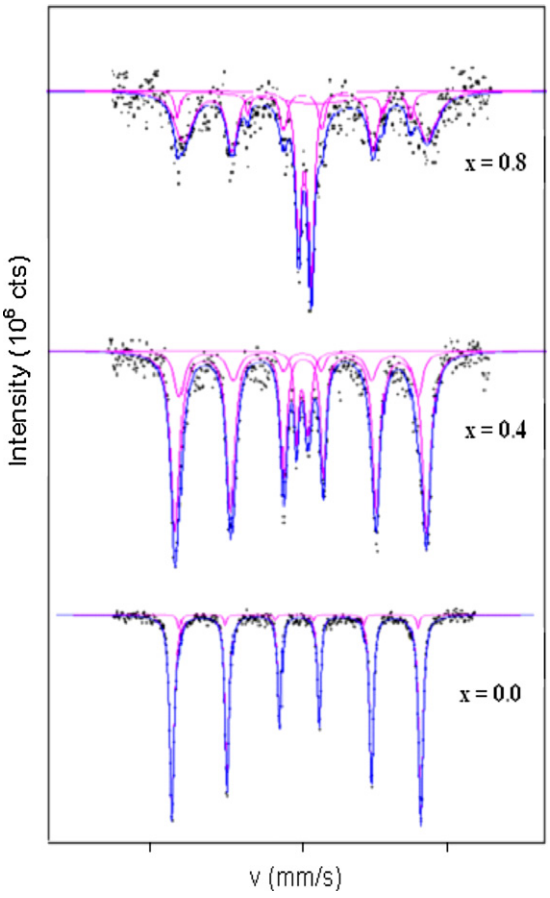

Fig. 7. Mossbauer spectra for $NiFe_{2-x}Sb_xO_4$ (a) $x = 0.0$, (b) $x = 0.4$ and (c) $x = 0.8$.

at B-site as compared to A-site as we move from $x = 0.0$ to $x = 0.8$. This indicates that antimony (Sb^{3+}) has a strong octahedral (B-site) preference.

The DC electrical resistivity (ρ) and the drift mobility (μ_d) of all the synthesized samples are measured by a two point probe method in the temperature range of 60–210 °C. The temperature dependence of the DC electrical resistivity and drift mobility for all the synthesized samples is shown in Figs. 8 and 9, respectively. It is observed that resistivity decreases in the whole temperature range for sample $x = 0.0$ like most of the ferrites materials reported in literature. The resistivity shows the interesting behavior with temperature for the substituted samples. The substituted samples

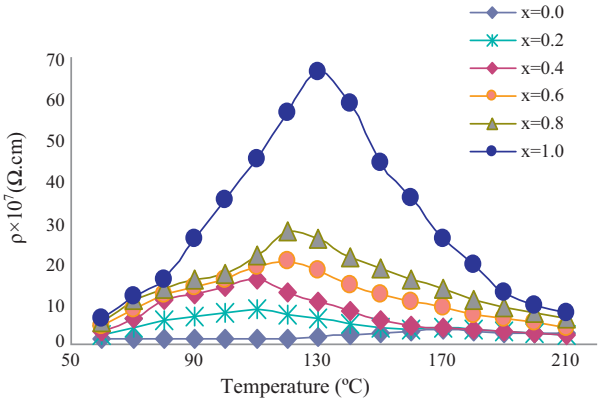

Fig. 8. Variation of DC electrical resistivity with temperature for all the synthesized samples.

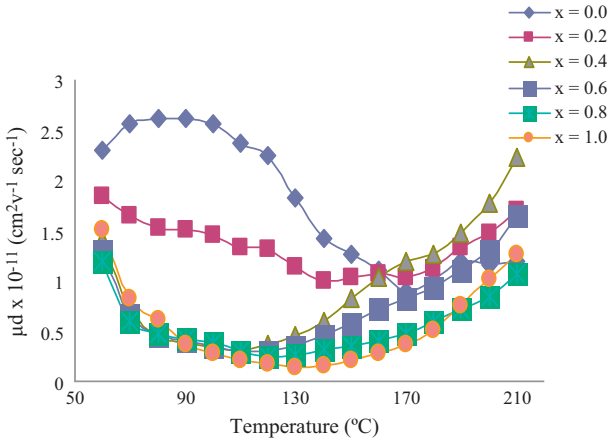

Fig. 9. Drift mobility of $NiFe_{2-x}Sb_xO_4$ as a function of temperature.

showed that the resistivity increases in the beginning, behaving like metal, reaches at a maximum value at a specific temperature and then decreases with further increase in the temperature behaving like semiconductors (Fig. 8). The temperature at which the transition occurs is named as metal-to-semiconductor transition temperature (T_{M-S}). It indicates that these materials may be used for switching applications. Such resistivity-temperature behavior is also reported earlier for Zr–Cu substituted M-type strontium hexaferrites [26] and Al–Cr substituted spinel ferrites [29]. The value of T_{M-S} is found to increase with the increase in the substitution of antimony as shown in Table 1. Such resistivity-temperature behavior in the present study may be attributed to the presence of some impurities, cation migration, spin canting and cation reordering. In present case there is no such possibility for the presence of any impurity as it is already confirmed by the XRD analysis. The cation migration at such low temperature (110–160 °C) in also not much rapid to give rise to the observed behavior but cannot be excluded. The only other possibility can be the spin canting because with the variation in the substitution and temperature the spin canting angles might change and this may be responsible for such resistivity-temperature behavior.

The temperature dependence of the drift mobility (μ_d) is shown in Fig. 9. The variation of the drift mobility (μ_d) with the temperature shows an opposite behavior to that of the DC electrical resistivity. The drift mobility is found to decrease below the metal-to-semiconductor transition temperature (T_{M-S}) and then above T_{M-S} drift mobility increases due to the decrease in the DC electrical resistivity.

The variation of the room temperature resistivity (ρ) and the drift mobility (μ_d) as a function of antimony content is shown in Fig. 10. The DC electrical resistivity is found to increase while the

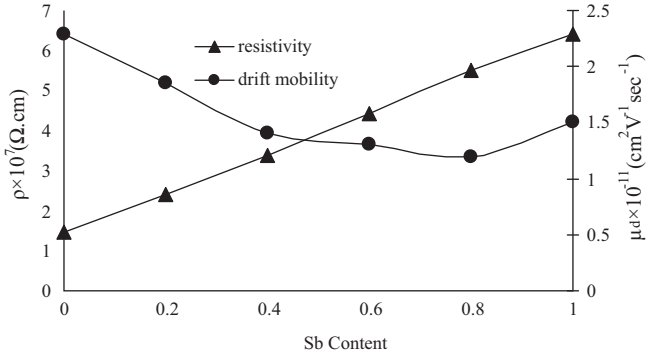

Fig. 10. Room temperature of DC electrical resistivity as a function of Sb content.

drift mobility decreases with an increase in the antimony content. The mechanism of conduction in ferrites is due to the hopping of electrons between ferrous (Fe^{2+}) and ferric (Fe^{3+}) at the octahedral site [31]. In the present work, it has been observed by the results obtained from the Mossbauer spectra that antimony (Sb^{3+}) predominantly occupies the octahedral site which is responsible for such behavior. Due to the replacement of iron by antimony from the octahedral site, the number of Fe^{3+} ions at the octahedral site decreases and hence the hopping of electrons also decreases. This results in an increase in the resistivity of the synthesized material. The variation in DC electrical resistivity is also related to the hopping of polarons generated by the conversion of Sb^{3+} into Sb^{5+} [32] at the octahedral site. This hopping of polarons hinders the movement of the charge carriers thus increasing the resistivity of the synthesized material. The increase in resistivity suggests that the synthesized materials can be used for applications in microwave devices as these devices require highly resistive materials.

4. Conclusion

Reverse microemulsion method has been adopted for the synthesis of nickel ferrite nanoparticles and its derivate. The single spinel phase of the synthesized samples is confirmed by the XRD analysis. The crystallite sizes estimated by the Scherrer's formula were in the range of 8–38 nm which is in agreement with 5–45 and 10–45 nm, calculated by AFM and SEM, respectively. Mossbauer spectra revealed that Sb^{3+} has a strong octahedral site preference. Substitution of Sb^{3+} causes remarkable changes in the structural and electrical properties of the spinel nickel ferrite. The variation in DC electrical resistivity as a function of temperature shows a metal-to-semiconductor transition temperature T_{M-S} which is beneficial in switching applications. The DC electrical resistivity increases while drift mobility decreases with the antimony content, which reveals that the synthesized materials have variety of applications in microwave devices.

Acknowledgement

The author (M.N. Ashiq) is thankful to the higher education commission (HEC) of Pakistan for financial support under project No. 20-1515/R&D/09-8049.

References

[1] D.S. Mathew, R.S. Juang, Chem. Eng. J. 129 (2007) 51.
[2] H. Gleiter, Prog. Mater. Sci. 33 (1989) 223.
[3] J.H. Fendler, Chem. Rev. 87 (1987) 877.
[4] M.P. Pileni, Adv. Funct. Mater. 5 (2001) 323.
[5] F.Y. Cheng, C.H. Su, Y.S. Yang, C.S. Yeh, C.Y. Tsai, C.L. Wu, M.T. Wu, D.B. Shieh, Biomaterials 26 (2005) 729.
[6] Q. Song, Z.J. Zhang, J. Am. Chem. Soc. 126 (2004) 6164.
[7] J. Sun, Sh. Zhou, P. Hou, Y. Yang, J. Weng, X. Li, M. Li, J. Biomed. Mater. Res. A 80 (2007) 333.
[8] R. Peelamedu, C. Grimes, D. Agrawal, R. Roy, J. Mater. Res. 18 (2003) 2292.
[9] A.K.M.A. Hossain, M. Seki, T. Kawai, H. Tabata, J. Appl. Phys. 96 (2004) 1273.
[10] M.S. Niasari, F. Davar, T. Mahmoudi, Polyhedron 28 (2009) 1455.
[11] T. Hyeon, Y. Chung, J. Park, S.S. Lee, Y.W. Kim, B.H. Park, J. Phys. Chem. B 106 (2002) 6831.
[12] G. Xiong, Z. Mai, M. Xu, S. Cui, Y. Ni, Z. Zhao, X. Wang, L. Lu, Chem. Mater. 13 (2001) 1943.
[13] L.J. Cote, A.S. Teja, A.P. Wilkinson, Z.J. Zhang, J. Mater. Res. 17 (2002) 2410.
[14] Z.J. Zhang, Z.L. Wang, B.C. Chakoumakos, J.S. Yin, J. Am. Chem. Soc. 120 (1998) 1800.
[15] A. Cabanas, M. Poliakoff, J. Mater. Chem. 11 (2001) 1408.
[16] C.T. Seip, E.E. Carpenter, C.J. O'Connor, V.T. John, S. Li, IEEE Trans. Magn. 34 (1998) 1111.
[17] M.J. Iqbal, M.N. Ashiq, I.H. Gul, J. Magn. Magn. Mater. 322 (2010) 1720.
[18] R.D. Waldron, Phys. Rev. 99 (1955) 1727.
[19] M.S. Niasare, F. Davar, T. Mahmoudi, Polyhedron 28 (2009) 1455.
[20] M. Srivastava, A.K. Ojha, S. Chaubey, A. Materny, J. Alloys Compd. 481 (2009) 515.
[21] S. Balaji, R.K. Selvan, L.J. Berchmans, S. Angappan, K. Subramanian, C.O. Augustin, Mater. Sci. Eng. B 119 (2005) 119.
[22] I.H. Gul, A. Maqsood, J. Alloys Compd. 465 (2008) 227.
[23] S. Mishra, T.K. Kundu, K.C. Barick, D. Bahadur, D. Chakravorty, J. Magn. Magn. Mater. 307 (2006) 222.
[24] I.H. Gul, F. Amin, A.Z. Abbasi, M.A. Rehman, A. Maqsood, Scripta Mater. 56 (2007) 497.
[25] S. Che, J. Wang, Q. Chen, J. Phys.: Condens. Matter 15 (2003) L335.
[26] M.J. Iqbal, M.N. Ashiq, P.H. Gomez, J.M. Munoz, J. Magn. Magn. Mater. 320 (2008) 881.
[27] H. Tang, Y.W. Du, Z.Q. Qiu, J.C. Walker, J. Appl. Phys. 63 (1998) 4105.
[28] L. Zhao, W. Xu, H. Yang, L. Yu, Curr. Appl. Phys. 8 (2008) 36.
[29] U.V. Chhaya, R.G. Kulkarni, Mater. Lett. 39 (1999) 91.
[30] A. Lakshman, P.S.V.S. Rao, K.H. Rao, Mater. Lett. 60 (2006) 7.
[31] A. Lakshman, P.S.S. Rao, B.P. Rao, K.H. Rao, J. Appl. Phys. 32 (2005) 673.
[32] P. Brahma, S. Banerjee, S. Chakraborty, D. Chakravoty, J. App. Phys. 88 (2000) 6526.